# *Ab initio* study of interelectronic correlations in electron-impact ionization of hydrogen

Daiji Kato and Shinichi Watanabe
*Department of Applied Physics and Chemistry, University of Electro-Communications, 1-5-1 Chofu-ga-oka, Chofu-shi, Tokyo 182, Japan*
(Received 15 May 1997)

Electron-impact ionization of hydrogen is investigated based upon *ab initio* quantal calculations. In the present calculations, strong interelectronic correlations are represented by the hyperspherical channel functions and accurate numerical solutions of the two-electron atomic Schrödinger equation are obtained by means of the smooth-variable-discretization method in combination with the $R$-matrix propagation method. The double-continuum boundary condition is represented by matching the numerical solutions to asymptotic solutions, which are described by superpositions of approximate asymptotic channel functions. We obtained the ionization threshold law, which is in good agreement with Wannier's conjecture, and also an almost uniform energy distribution in double-continuum states at low energies, say $\sim 0.1$ a.u. At low energies, the angular distributions of the electrons in double-continuum states of $^1S^e$ localize where the interelectronic angular distance $\theta_{12}=\pi$. As the energy increases, the binary-encounter and the dipolelike transition mechanisms manifest themselves in the angular distribution. The spin-averaged total ionization cross section and the spin asymmetry from the present method agree well with experimental measurements as well as the convergent-close-coupling result, while for the spin asymmetry there is a noticeable disagreement with the hidden-crossing result at moderately low energies. An essential role of the potential *ridge* during the ionization process is apparent in the convergence of the present calculations. [S1050-2947(97)02611-5]

PACS number(s): 34.50.Fa, 34.80.Dp

## I. INTRODUCTION

Electron-impact ionization of hydrogen is a basic atomic process that leads to disintegration of one heavy and two light Coulombic particles. The disintegrated state is frequently referred to as the double-continuum state

$$e^- + \mathrm{H} \rightarrow e^- + e^- + p^+. \tag{1}$$

The bulk of the ionization cross sections that provide important information for plasma physics, for example, are distributed in a high- to intermediate-energy range. At high energies, the time spent by the incident electron in an effective range of the interaction potential should be even smaller than a characteristic time for the potential to have a significant effect. Indeed, perturbative treatments were applicable in this energy range [1]. At intermediate energies where the ionization cross section has a maximum, the convergent-close-coupling method of Bray and Stelbovics [2] has succeeded in bridging a gap between theoretical predictions and experimental measurements for the ionization cross section.

However, theoretical interests are rather strong on the low-energy side because what has been attracting the interest of atomic theoretists is the interelectronic correlations in double-continuum states that become pronounced at low energies. In particular, the correlations manifest themselves in the threshold law of the ionization cross section: The threshold law is frequently described by $E^\eta$, where $E$ is the energy excess from the ionization threshold. Wannier's famous theory [3] provides the exponent $\eta \simeq 1.127$ for the electron-impact ionization of neutral atoms. In his theory, the threshold ionization paths are presumably represented by specific classical trajectories that correspond to correlated motions of the two electrons astride the potential *ridge*, namely, $r_1 = r_2$ and $\theta_{12}=\pi$, where $r_1$ and $r_2$ are radial distances of individual electrons and $\theta_{12}$ is the angular distance between the two electrons. The value of the exponent ($\simeq 1.127$) is associated with the Lyapunov-type exponent of the above-mentioned specific classical trajectories. Later, semiclassical and quantal local solutions that correspond to Wannier's classical trajectories were found independently by Peterkop [4] and Rau [5]. Klar and Schlecht [6] applied Wannier's theory to the states of arbitrary values of the total angular momentum. Feagin [7] reformulated Wannier's theory for arbitrary masses and charges. A quantal calculation of the absolute cross sections for electron-impact ionization of helium near the first-ionization threshold was made by Crothers [8] using Peterkop's solutions. Other theoretical efforts [9] also have been made to examine the threshold law; however, all of them largely resorted to Wannier's conjecture. On the other hand, experimental efforts to determine the threshold exponent also exist. McGowan and Clarke [10] measured relative ionization cross sections for electron-impact ionization of hydrogen in energy range up to a few hundreds of meV from the threshold. They obtained the value $1.13 \pm 0.03$ for the exponent. Later, Cvecjanović and Read [11] determined the exponent with a carefully designed apparatus for electron-impact ionization of helium and obtained the value $1.131 \pm 0.019$. Both of the measurements are consistent with Wannier's threshold law. Since then, Wannier's conjecture has been largely accepted by atomic physicists.

Nevertheless, it is nontrivial to obtain the threshold law theoretically without recourse to Wannier's conjecture because of difficulties in the *ab initio* treatment of interelectronic correlations in double-continuum states. In this regard, we must mention some existing theories. Proulx and Shakeshaft [12] calculated the absolute cross section for double-photoionization of helium by means of an *ab initio* basis-set

 

method, but with the aid of some semiclassical ansatz for final-state wave functions. Their result is consistent with the conjecture of Wannier's theory for the double photoionization of helium. Rost [13] applied the semiclassical $S$-matrix theory for the threshold ionization of the electron-hydrogen collision, in particular for a collinear model in which the motions of the two electrons are restricted in a line with the nucleus between them. In Rost's theory, the ionization dynamics is represented solely by the classical trajectories of the two electrons. He obtained an ionization cross section that is consistent with Wannier's threshold law. Recently, Macek *et al.* [14] applied the hidden-crossing theory to the threshold ionization of electron-hydrogen collision. They deduced the Wannier-Peterkop-Rau solution approximately by means of the angle Sturmian basis expansion; the hidden-crossing theory provided the threshold exponent $\simeq 1.104$ using only one angle Sturmian basis.

For further insight into details of ionization dynamics, the energy distribution as well as the angular distribution of the two electrons in double-continuum states are important subjects to be investigated. In particular, for the energy distribution, experimental measurements [11,15] provided an almost uniform distribution near the threshold. However, the local solutions of Peterkop and Rau are not capable of explaining the uniform energy distribution. Feagin obtained a Gaussian distribution peaked at $\epsilon_1 = \epsilon_2$, where $\epsilon_1$ and $\epsilon_2$ are the energies of the individual electrons, by means of the fourth-order Wannier theory [16] in which the interaction potential are expanded up to the fourth order around the ridge. The point is that the Wannier-Peterkop-Rau solution is valid only near $r_1 = r_2$, though to obtain the correct energy distribution it is necessary to take the whole radial coordinate space into account. On the other hand, Vinkalns and Gailitis [17] carried out a classical trajectory calculation and obtained an almost uniform energy distribution. Other classical trajectory calculations [13,18], a semiclassical calculation [19], and quantal calculations aided by a semiclassical ansatz [20,21] also provided the almost uniform energy distribution. Is the correct energy distribution really uniform at low energies? No existing theory appears to be in a position to provide a full quantal answer.

The purpose of this paper is an *ab initio* study of the threshold law as well as the energy and the angular distribution based upon fully quantal calculations. To this end, the hyperspherical adiabatic channel functions are exploited to represent strong interelectronic correlations rigorously. Accurate numerical solutions of the two-electron atomic Schrödinger equation are obtained by means of the smooth-variable-discretization method [22] in combination with the $R$-matrix propagation method [23]. In order to impose the double-continuum boundary condition on the solutions, we match the hyperspherical solutions to some asymptotic solutions on a fixed hyper-radius, which is subsequently referred to as the matching hyperradius. However, a principal problem here is that we do not know any exact analytical expressions representing asymptotic solutions for double-continuum states. Instead, in this paper, approximate asymptotic channel functions, each of which is represented simply by a product of a pseudohydrogenic target wave function and a free scattering wave function, are employed [24]. The double-continuum components are specified as the residue after subtracting from the total wave function the excitation components, the latter components being better defined since the asymptotic channel functions satisfy the well-defined excitation boundary condition. In actual implementations, the target states that involve discrete as well as continuum spectra of the target atom are discretized by confining the target wave functions within a sphere whose finite radius is determined from the matching hyperradius. The discretization procedure is required not only for representing the continuum spectrum effectively, but also for defining the normalization of the asymptotic channel functions on the hypersphere of a given matching hyperradius. The technical problems being resolved in this manner, we are in a position to explore the physics of electron-impact ionization of hydrogen at relatively low energies on the basis of quantum mechanics.

This paper is organized as follows. We describe the present theoretical method in Sec. II. An accurate numerical method for solving the two-electron atomic Schrödinger equation is given in Sec. II A. Section II B is devoted to describing the asymptotic solutions and to specifying ionization components. In Sec. III we analyze theoretical results. In Secs. III A and III B the ionization threshold law and the energy distribution of the two electrons in double-continuum states are examined in a model in which the angular degrees of freedom are frozen, while the radial degrees of freedom are taken into account completely. An important role of the potential ridge during the ionization process becomes apparent by analyzing the convergence of the present calculations (Sec. III C). The angular correlations of double-continuum states are examined within the $^1S^e$ symmetry in Sec. III D. From the angular distributions that are obtained from *ab initio* ionization wave functions, ionization mechanisms are investigated in a wide energy range. In Sec. III E we demonstrate the validity of the present theoretical method by comparison of the spin-averaged total ionization cross sections as well as the spin asymmetry with experimental measurements and other theoretical results in the low- to intermediate-energy range. In Sec. IV we conclude the paper.

## II. THEORETICAL METHOD

### A. Accurate numerical solution of the two-electron atomic Schrödinger equation

#### *1. Hyperspherical coordinates and adiabatic expansion*

The Schrödinger equation for a two-electron atom is

$$\left[ -\frac{1}{2}\nabla_1^2 - \frac{1}{2}\nabla_2^2 - \frac{Z}{r_1} - \frac{Z}{r_2} + \frac{1}{r_{12}} - E \right] \Psi(\vec{r}_1, \vec{r}_2) = 0, \quad (2)$$

where $\nabla^2$ represents the Laplacian operator, $\{r_1, r_2\}$ are the radial coordinates of the two electrons, $r_{12}$ is the interelectronic distance, and $Z$ is the nuclear charge. Atomic units are used throughout ($\hbar = m_e = 1$) unless otherwise stated. The representation of the system by the independent-particle coordinates suffers a slow convergence from strong interelectronic correlations. Instead, we represent the system by the hyperspherical coordinates that are suited for describing the interelectronic correlations.

In the hyperspherical coordinates, the Schrödinger equation reads

$$\left[-\frac{1}{2}R^{-5}\frac{\partial}{\partial R}R^5\frac{\partial}{\partial R}+\frac{1}{R^2}\left(\frac{1}{2}\Lambda^2(\Omega)+RC(\Omega)\right)-E\right]\times\Psi(R,\Omega)=0, \tag{3}$$

where the hyperradius $R$ represents the mean-square radius of the system, namely, $\sqrt{r_1^2+r_2^2}$, and $\Omega$ groups five residual angular coordinates, namely, $(\alpha=\arctan(r_2/r_1),\hat{r}_1,\hat{r}_2)$. The grand-angular momentum operator $\Lambda^2(\Omega)$ and the effective charge $C(\Omega)$ are

$$\Lambda^2(\Omega)=-\frac{1}{\sin^2 2\alpha}\frac{\partial}{\partial\alpha}\sin^2 2\alpha\frac{\partial}{\partial\alpha}-\frac{L_1^2}{\sin^2\alpha}-\frac{L_2^2}{\cos^2\alpha},$$

$$L_i^2=\frac{1}{\sin\theta_i}\frac{\partial}{\partial\theta_i}\sin\theta_i\frac{\partial}{\partial\theta_i}+\frac{1}{\sin^2\theta_i}\frac{\partial^2}{\partial\phi_i^2}, \tag{4}$$

$$C(\Omega)=-\frac{Z}{\sin\alpha}-\frac{Z}{\cos\alpha}+\frac{1}{\sqrt{1-\sin 2\alpha\cos\theta_{12}}},$$

where $\theta_{12}$ is the interelectronic angular distance. Adiabatic separability of the system with respect to the hyperradius becomes apparent in the hyperspherical coordinates [25]. The adiabatic Hamiltonian operator is

$$H_{ad}(\Omega;R)=\frac{1}{2}\Lambda^2(\Omega)+RC(\Omega). \tag{5}$$

Adiabatic states provide a convergent representation of correlated motions of two electrons on the hypersphere of a given hyperradius $R$. In the present calculations, solutions of the two-electron atomic Schrödinger equation are thus expanded in terms of adiabatic channel functions that are obtained by diagonalizing the adiabatic Hamiltonian operator. More specifically, in the present calculations the adiabatic channel functions are represented by

$$\Phi_n(\Omega;R)=\sum_a (1-x)^{l_2+1}(1+x)^{l_1+1}P_i^{2l_2+1,2l_1+1}(x)\times\mathcal{Y}_{l_1l_2JM}(\hat{r}_1,\hat{r}_2)C_{an}(R), \tag{6}$$

where $x\,[=(4/\pi)\alpha-1]\in[-1,1]$, $a=\{il_1l_2\}$,$\{P_i^{2l_2+1,2l_1+1}\}$ are the Jacobi polynomials, and $\{\mathcal{Y}_{l_1l_2JM}\}$ represents the coupled angular momentum states. A set of coefficients $\{C_{an}(R)\}$ is determined by the diagonalization of the adiabatic Hamiltonian operator in the representation of $\{P_i^{2l_2+1,2l_1+1}\}\times\{\mathcal{Y}_{l_1l_2JM}\}$. In this representation, solutions readily converge with respect to $\alpha$ once the angular configurations $\{l_1,l_2\}$ are fixed. However, the individual angular configurations are coupled due to the interelectronic interaction potential $1/r_{12}$. The convergence with respect to the angular configuration is examined in Sec. III D, which concerns the angular correlations of the two electrons in double-continuum states.

#### 2. Stable propagation of the solutions in the $\mathcal{R}$-matrix form

The hyperspherical coordinates consist of one noncompact variable that is the hyperradius $R\in[0,\infty]$ and the other compact variables $\Omega$. Systems bounded in a finite range provide well-defined eigenvalue problems. Thus we divide the hyperradius into finite intervals, calculate solutions within each interval, and then propagate them with respect to the hyperradius so as to construct globally continuous and smooth solutions. This section is devoted to the mathematical formulation of the $\mathcal{R}$-matrix propagation method [23].

Scaling the solutions as $\psi=R^{3/2}\Psi$ leads to the Schrödinger equation

$$\left[-\frac{1}{2}\frac{\partial}{\partial R}R^2\frac{\partial}{\partial R}+\frac{15}{8}+\frac{1}{2}\Lambda^2(\Omega)+RC(\Omega)-R^2E\right]\psi(R,\Omega)=0. \tag{7}$$

The Bloch operator is then introduced in a finite interval $[a,b]$,

$$\mathcal{L}(R)=R^2\left[\delta(R-b)\frac{\partial}{\partial R}-\delta(R-a)\frac{\partial}{\partial R}\right], \tag{8}$$

so that $H(R,\Omega)+\mathcal{L}(R)$ becomes Hermitian in the interval, where

$$H(R,\Omega)=-\frac{1}{2}\frac{\partial}{\partial R}R^2\frac{\partial}{\partial R}+\frac{15}{8}+\frac{1}{2}\Lambda^2(\Omega)+RC(\Omega). \tag{9}$$

The solutions $\psi$ are formally written using the Green's function

$$\psi(R,\Omega)=\int_a^b dR'\int d\Omega'\mathcal{G}(R,\Omega;R',\Omega')\mathcal{L}(R')\psi(R',\Omega'). \tag{10}$$

A spectral resolution of the Green's function is constructed,

$$\mathcal{G}(R,\Omega;R',\Omega')=\sum_k\frac{u_k(R,\Omega)u_k(R',\Omega')}{E_k-E}, \tag{11}$$

where $\{u_k(R,\Omega),E_k\}$ is a set consisting of the solutions and the corresponding eigenvalues of

$$[H(R,\Omega)+\mathcal{L}(R)-R^2E_k]u_k(R,\Omega)=0, \tag{12}$$

which is defined within the interval $[a,b]$. It is nontrivial to solve such multidimensional eigenvalue problems with a high precision. An accurate method for solving this type of multidimensional eigenvalue problem is presented in Sec. II A 3. Substituting the spectral resolution of the Green's function into Eq. (10), we obtain an expression for the solutions in the form

$$\psi(R,\Omega)=\sum_k\frac{u_k(R,\Omega)}{E_k-E}\left[b^2\left\langle u_k\left|\frac{\partial\psi}{\partial R}\right\rangle_{R=b}-a^2\left\langle u_k\left|\frac{\partial\psi}{\partial R}\right\rangle_{R=a}\right.\right], \tag{13}$$

where $\langle|\rangle$ represents the integration over $\Omega$.

We represent the solutions in terms of the adiabatic channel functions $\{\Phi_n(\Omega;R)\}$, which constitute an orthonormal basis set at each hyperradius. Then the $\mathcal{R}$ matrix with respect to the adiabatic channels is defined at both boundaries of the interval as

$$\langle\Phi_n|\psi\rangle_{R=a}=a\sum_m \mathcal{R}_{nm}(a)\left\langle \Phi_m\left|\frac{\partial\psi}{\partial R}\right\rangle_{R=a}\right.,$$

$$\langle\Phi_n|\psi\rangle_{R=b}=b\sum_m \mathcal{R}_{nm}(b)\left\langle \Phi_m\left|\frac{\partial\psi}{\partial R}\right\rangle_{R=b}\right.. \tag{14}$$

From Eqs. (14) and (13) the $\mathcal{R}$-matrix propagation formula is obtained in the form

$$b\mathcal{R}_{nm}(b)=G^{bb}_{nm}-\sum_l\sum_{l'} G^{ba}_{nl}[G^{aa}+a\mathcal{R}(a)]^{-1}_{ll'}G^{ab}_{l'm}, \tag{15}$$

where

$$G^{R_1R_2}_{nm}=R_1R_2\sum_k \frac{\langle\Phi_n(R_1)|u_k(R_1)\rangle\langle u_k(R_2)|\Phi_m(R_2)\rangle}{E_k-E}. \tag{16}$$

The $\mathcal{R}$ matrix is uniquely fixed at all values of the hyperradius once the boundary condition of the regular solutions at $R=0$ is applied. Thus the $\mathcal{R}$ matrix is first set to zero at $R=0$. The performance of the propagation method is very stable since the numerical collapse due to exponentially increasing or decreasing solutions does not occur in the $\mathcal{R}$-matrix form. Moreover, the propagators for different energies can be readily constructed once the eigenvalue problem of Eq. (12) is solved.

### *3. Rigorous treatment of the nonadiabatic coupling by smooth-variable-discretization method*

Now we consider the eigenvalue problem of Eq. (12). In the adiabatic representation of the solutions, we obtain a set of coupled ordinary differential equations (ODEs) with respect to the hyperradius. In the ODEs, nonadiabatic couplings among the adiabatic states are represented by $\langle\Phi_n|\partial\Phi_{n'}/\partial R\rangle$ whose elements sharply peak at avoided crossings of the adiabatic potential curves. It is quite cumbersome to handle such sharp variations of the couplings since the avoided crossings occur rather randomly.

To avoid laborious evaluations of the nonadiabatic couplings, the diabatic-by-sector method [26] was developed in calculations of atom-molecule collisions; the method has been applied frequently to atomic physics problems [27]. The diabatic-by-sector representation of the solutions does not require an explicit evaluation of the nonadiabatic couplings. Instead, the method incorporates the nonadiabatic couplings into matrix elements of the adiabatic Hamiltonian operator in the representation

$$\langle\Phi_n(R_m)|H_{ad}(R)|\Phi_{n'}(R_m)\rangle, \tag{17}$$

where $\{\Phi_n(R_m)\}$ represents the set of diabatic-by-sector basis functions defined at the midpoint of the interval $[a,b]$. However, even in the limit $\Delta R\ (=b-a)\to 0$, the representative Hilbert space of the diabatic-by-sector solutions does not span as much solution space as does the adiabatic expansion with the same number of adiabatic channels [28], and the situation becomes even worse in exotic atomic systems such as $dt\mu$ [22]. Thus convergence must be achieved only by increasing the number of diabatic-by-sector basis functions in the calculations. This leads to a sizable calculation, which should be avoided.

Recently, the smooth-variable-discretization (SVD) method was introduced by Tolstikhin *et al.* [22] to treat the nonadiabatic couplings rigorously without labored calculations. The SVD method treats the Schrödinger equation in the discrete-variable-representation (DVR) [29] with respect to $R$ and in the adiabatic channel representation with respect to $\Omega$. Though the complete mathematical formulation of the SVD method was presented in the original paper by Tolstikhin *et al.*, we reproduce the gist of the formulation for the present implementation.

We introduce a set of orthonormal basis functions within the interval $[a,b]$,

$$\varphi_i(R)=\sqrt{w(x)/h_{i-1}}P^{\alpha,\beta}_{i-1}(x),$$

$$x=(a-b-2R)/(a-b)\in[-1,1], \tag{18}$$

where $\{P^{\alpha,\beta}_{i-1}(x)\}$ are Jacobi polynomials and $w(x)$ and $h_{i-1}$ are their weight function and normalization constants, respectively. In this paper we set $\alpha=0$ and $\beta=3$ for the initial interval $[0,\Delta R]$ in order to take the nonanalyticity $R^{3/2}$ of the solutions at $R=0$ into account and set $\alpha=\beta=0$ for the other intervals so that the basis functions represent arbitrary boundary conditions. Using the basis functions $\{\varphi_i(R)\}$, we define a set of DVR basis functions $\{\pi_j(R)\}$ within an $M$-dimensional subspace $\mathcal{H}^{(M)}$ by

$$\varphi_i(R)=\sum_j^M T_{ij}\pi_j(R), \tag{19}$$

where

$$T_{ij}=(T^{-1})_{ji}=\kappa_j\varphi_i(R_j),\quad \kappa_j=\sqrt{W_j/w(x_j)}, \tag{20}$$

where $R_j, W_j$ are the quadrature abscissas and weights of $P^{\alpha,\beta}_M(x)$. The orthogonality of $T_{ij}$ is readily deduced from the Christoffel-Darboux identity. The DVR basis functions have an important property, namely, $\pi_j(R_{j'})=\kappa_j^{-1}\delta_{jj'}$.

Then the solutions are expanded in terms of the DVR basis functions as

$$u_k(R,\Omega)=\sum_{j=1}^M \pi_j(R)\Theta_{jk}(\Omega). \tag{21}$$

A set of coupled ordinary differential equations with respect to the coefficients $\{\Theta_{jk}(\Omega)\}$ reads

$$H_{ad}(\Omega;R_j)\Theta_{jk}(\Omega)+\sum_{j'=1}^M [K_{jj'}-\rho_{jj'}E_k]\Theta_{j'k}(\Omega)=0, \tag{22}$$

where

$$K_{jj'}=\int_a^b \pi_j(R)\left(-\frac{1}{2}\frac{\partial}{\partial R}R^2\frac{\partial}{\partial R}+\frac{15}{8}+\mathcal{L}(R)\right)\pi_{j'}(R)dR,$$

$$\rho_{jj'}=\int_a^b \pi_j(R)R^2\pi_{j'}(R)dR. \tag{23}$$

This is the DVR representation of the Schrödinger equation in $\mathcal{H}^{(M)}$. Then we represent the coefficients in terms of the adiabatic channel functions, namely, the adiabatic expansion,

$$\Theta_{jk}(\Omega)=\sum_n \Phi_n(\Omega;R_j)c_{njk}. \tag{24}$$

A set of coefficients $\{c_{njk}\}$ is determined by solving the algebraic generalized eigenvalue problem

$$U_\nu(R_j)c_{njk}+\sum_n\sum_{j'=1}^{M}[K_{jj'}-\rho_{jj'}E_k]O_{nj,n'j'}c_{n'j'k}=0, \tag{25}$$

where $O_{nj,n'j'}$ represent the overlap of the adiabatic channel functions at different values of the hyperradial distances $\langle\Phi_n(R_j)|\Phi_{n'}(R_{j'})\rangle$. The nonadiabatic couplings are incorporated into the overlap matrix elements implicitly. The SVD solutions principally coincide with those of the adiabatic expansion of the same order as long as the DVR representation of the Schrödinger equation with respect to $R$ is valid. Indeed, the convergence of the SVD solutions is fast since the Schrödinger equations of Coulomb three-body systems are quite smooth with respect to $R$ [see Eq. (7)].

### B. Asymptotic boundary condition

In this section we explain how to represent the asymptotic solutions of the Schrödinger equation and how to extract the ionization components. The term ''asymptotic'' here means the region where the kinetic energy of the two electrons dominates over the Coulomb interaction potential. Therefore, in terms of the hyperradius, the asymptotic region is characterized by $R\gg E^{-1}$. Excitation as well as ioinization is presumably completed when the asymptotic region is reached since the two electrons hardly exchange their kinetic energies thereafter. Thus the asymptotic solutions are described by the independent-particle coordinates. There is another reason why the independent-particle representation should be applied in the asymptotic region. Disintegration of atomic systems, that is, ionization, is hardly specified in terms of the hyperspherical adiabatic channels [30] because all adiabatic channels converge to excitation channels asymptotically as $R\to\infty$. Disintegration channels are readily specified in the independent-particle representation.

#### *1. Asymptotic solutions*

In this paper the asymptotic channel functions are represented by direct products of independent-particle solutions

$$\phi_a(\vec{r}_1,\vec{r}_2)=R^{-1/2}f_{kl_1}(r_1)g_{\epsilon l_2}(r_2)\mathcal{Y}_{l_1l_2JM}(\hat{r}_1,\hat{r}_2),\quad r_1>r_2, \tag{26}$$

where $a=\{\epsilon l_1 l_2\}$ and $E=k^2/2+\epsilon$. In the subsequent discussion we consider only a half triangle of the radial coordinate space, which is described by $r_1>r_2$. The other half triangle, $r_2>r_1$, is taken into account through the antisymmetrization condition, that is, $\phi(\vec{r}_1,\vec{r}_2)=(-1)^S\phi(\vec{r}_2,\vec{r}_1)$ where $S$ is the total spin of the two electrons. The factor $R^{-1/2}$ in Eq. (26) is necessary for representing the $R^{3/2}$ behavior of the solutions at $R=0$.

The target wave functions $\{g_{\epsilon l_2}(r_2)\}$, which correspond to discrete as well as continuum states of the target atom, are solutions of the hydrogenic Schrödinger equation within a finite radial interval $[0,R_M/\sqrt{2}]$, where $R_M$ represents the matching hyperradius where the numerically obtained interior solutions are matched to the asymptotic ones. We subsequently refer to the interior solutions as the hyperspherical solutions because they are represented in terms of the hyperspherical adiabatic channel functions. We discretize the target continuum states by the boundary condition

$$g_{\epsilon l_2}(0)=g_{\epsilon l_2}(R_M/\sqrt{2})=0. \tag{27}$$

Then the solutions are normalized so that

$$\int_0^{R_M/\sqrt{2}}|g_{\epsilon l_2}|^2dr_2=1. \tag{28}$$

Due to the boundary condition, the wave function $\{g_\epsilon\}$ of highly excited states whose energies lie in $-\sqrt{2}/R_M<\epsilon<0$ do not coincide with the true hydrogenic wave function.

The functions $\{f_{kl_1}(r_1)\}$ represent solutions of the monopole Schrödinger equation

$$\left[-\frac{1}{2}\frac{d^2}{dr_1^2}+\frac{l_1(l_1+1)}{2r_1^2}-\frac{(Z-1)}{r_1}-\frac{k^2}{2}\right]f_{kl_1}(r_1)=0, \tag{29}$$

where the interelectronic Coulomb interaction $1/r_{12}$ is replaced by the monopole term $1/r_1$. Here $\{f^+_{kl_1}(r_1)\}$ represent the outgoing traveling waves and $\{f^-_{kl_1}(r_1)\}$ represent the incoming traveling waves; they are energy normalized and preserve the Wronskian $|f^+(df^-/dr_1)-f^-(df^+/dr_1)|$. Thus the two groups of the asymptotic channel functions are defined by $\{\phi^\pm_a\}=\{f^\pm_{kl_1}\}\times\{g_{\epsilon l_2}\}$. Evidently, the asymptotic channel functions $\{\phi^\pm_a\}$ are a crude approximation to exact asymptotic solutions of the two-electron atomic Schrödinger equation unless the multipole terms of the interelectronic interaction are entirely negligible. However, it is worth noting that the Wronskian of the asymptotic channel functions is preserved in this approximate representation. The Wronskian with respect to the hyperradius is

$$W_R=\left|R^2\int\int d\hat{r}_1d\hat{r}_2\int_0^{\alpha/4}d\alpha\left(\phi_a^+\frac{\partial\phi_a^-}{\partial R}-\phi_a^-\frac{\partial\phi_a^+}{\partial R}\right)\right|$$

$$=w_f\int_0^{R_M/\sqrt{2}}|g(r_2)|^2dr_2, \tag{30}$$

where $w_f=|f^+(df^-/dr_1)-f^-(df^+/dr_1)|$ is the Wronskian of $f^\pm(r_1)$. Using the normalization conditions of $f^\pm(r_1)$ and $g(r_2)$, we find that the Wronskian $W_R$ is preserved.

Asymptotic solutions that satisfy the outgoing wave boundary condition are represented by a superposition of the asymptotic channel functions

$$\psi_a^+ = \phi_a^- \delta_{aa'} + \sum_{a'} \phi_{a'}^+ C_{a'a}, \tag{31}$$

where the first term represents the incoming part and the second term represents the outgoing part of the solutions. Strictly speaking, the coefficients $\{C_{a'a}\}$ for the continuum states depend logarithmically on the hyperradius due to the long-range interelectronic interaction potential. However, we safely neglect the logarithmic dependence at a sufficiently large hyperradius. The set of coefficients are determined by matching the hyperspherical solutions to the asymptotic expression of Eq. (31) at $R_M \gg E^{-1}$. The matching condition is

$$\psi_a^+(R_M) = \sum_k \psi_k^{HS}(R_M) A_{ka}^+,$$

$$\frac{\partial \psi_a^+(R_M)}{\partial R} = \sum_k \frac{\partial \psi_k^{HS}(R_M)}{\partial R} A_{ka}^+, \tag{32}$$

where $\{\psi_k^{HS}\}$ represent the hyperspherical solutions. In Eq. (32) there are two sets of unknown coefficients, namely, $\{C_{a'a}\}$ and $\{A_{ka}^+\}$. Using the $\mathcal{R}$ matrix at the matching hyperradius, we obtain a set of equations for the coefficients $\{C_{a'a}\}$,

$$\langle \Phi_n | \psi_a^+ \rangle |_{R=R_M} = \sum_{n'} \mathcal{R}_{nn'} \left\langle \Phi_{n'} \left| \frac{\partial \psi_a^+}{\partial R} \right\rangle \right|_{R=R_M}. \tag{33}$$

Substituting the form of the asymptotic solutions (31) into Eq. (33), we obtain a set of algebraic equations for the coefficients $\{C_{a'a}\}$,

$$\sum_{a'} Z_{na'}^+ C_{a'a} = Z_{na}^-, \tag{34}$$

where

$$Z_{na}^{\pm} = \langle \Phi_n | \phi_a^{\pm} \rangle - \sum_{n'} \mathcal{R}_{nn'} \left\langle \Phi_{n'} \left| \frac{\partial \phi_a^{\pm}}{\partial R} \right\rangle \right. . \tag{35}$$

In the present paper the coefficient matrix $\mathbf{Z}^+$ always becomes rectangular because the order of the representative Hilbert space is different between the interior and the asymptotic representations. More specifically, more independent-particle solutions are required than the hyperspherical adiabatic channels to represent the correct solution space. Thus the algebraic system becomes overdetermined, namely, singular. Therefore, the direct inversion of the coefficient matrix is not applicable. The overdetermined algebraic system has more than one solution: Any solutions of the homogeneous equation $\mathbf{Z}^+\mathbf{x}=\mathbf{0}$ can be added to the solution. Thus we must effectively throw away singular solutions and extract the proper solutions.

We first diagonalize the coefficient matrix in the form

$$\mathbf{Z}^+ = \mathbf{U}\mathbf{w}\mathbf{V}^T, \tag{36}$$

where $\mathbf{U}$ is a column-orthogonal matrix, $\mathbf{V}$ is an orthogonal matrix, and $\mathbf{w}$ is a diagonal matrix whose elements represent singular values of the algebraic system. This is frequently called the singular-value decomposition [31]. Then the inverse of the coefficient matrix is formally written

$$(\mathbf{Z}^+)^{-1} = \mathbf{V}\mathbf{w}^{-1}\mathbf{U}^T, \tag{37}$$

where we use the orthogonality of $\mathbf{U}$ and $\mathbf{V}$. In case the algebraic system is almost singular, there are some vanishingly small singular values, that is, $w \simeq 0$, and their inverses become infinitely large. The column of $\mathbf{V}$ whose corresponding singular value is zero represents the solution of the homogeneous equation, namely, $\mathbf{x}$. Thus, by replacing the corresponding $w^{-1} \simeq \infty$ by zero, we obtain the desirable solution uniquely.

#### *2. Extraction of ionization components*

The above-mentioned procedure provides the set of coefficients $\{C_{a'a}\}$ that contain complete scattering information. The next step is to extract ionization information from the coefficients. In this work, the total flux is preserved within four significant digits, that is, $J_a = \Sigma_{a'} |C_{a'a}|^2 = 1$. The coefficients $\{C_{a'a}\}$ of each discrete target state $a'(\epsilon<0)$ are identical to the corresponding scattering matrix elements because the asymptotic channel functions satisfy the boundary condition for excitation. Thus the flux of excitation to each discrete target state is well represented by $J_{a' \leftarrow a} = |C_{a'a}|^2$. The excitation cross sections are readily obtained from $J_{a' \leftarrow a}$. However, the coefficients of continuum target states $a'(\epsilon>0)$ are different from the corresponding scattering matrix elements because the asymptotic channel functions are a crude approximation to the exact asymptotic continuum states [see Eq. (29)]. Nevertheless, since the flux conservation condition is satisfied in the present calculations, an ionization flux can be extracted by

$$J_{ion \leftarrow a} = J_a - \sum_{a'(\epsilon<0)} J_{a' \leftarrow a} = \sum_{a'(\epsilon>0)} |C_{a'a}|^2. \tag{38}$$

In the above equation the total excitation flux is represented by a summation of the flux over discrete target states, namely, $\Sigma_{a'(\epsilon<0)} J_{a' \leftarrow a}$. However, the flux of the highly excited states $a'(-\sqrt{2}/R_M < \epsilon < 0)$ is different from that of the true hydrogenic states. Thus a subtle uncertainty in the ionization flux remains as long as the matching hyperradius is finite. The uncertainty is suppressed only by increasing the matching hyperradius.

Similarly, an ionization wave function is represented by

$$\psi_{ion}^+ = \sum_{a'(\epsilon>0)} \phi_{a'}^+ C_{a'a}. \tag{39}$$

In the asymptotic region, a constraint $\Omega = \Omega_k$ is obtained within the validity of the stationary-phase approximation [4], where $\Omega_k = (\alpha_k = \arctan(k_2/k_1), \hat{k}_1, \hat{k}_2)$ and $\vec{k}_1$ and $\vec{k}_2$ are the individual momentum vectors of the two electrons. From the classical mechanical viewpoint, this means that the direction of the asymptotic momentum of each electron coincides with that of its radial vector asymptotically unless the two electrons exchange their kinetic energies. Since the energy ex-

change does not take place asymptotically, we can examine differential ionization cross sections using the relation

$$\frac{d\sigma_{ion}}{d\Omega_k} \propto |\psi^{+}_{ion}(\Omega_k)|^2. \tag{40}$$

However, near the potential *valley*, namely, $\alpha \sim 0$ or $\pi/2$, the relation of Eq. (40) is not applicable because there the stationary-phase approximation becomes invalid as long as the matching hyperradius is finite. Therefore, there remains an uncertainty for the normalization of the differential cross section. Thus, in this paper we examine only relative shapes for the differential cross sections using Eq. (40).

## III. RESULTS AND DISCUSSION

### A. Wannier exponent for the two-dimensional model

Wannier's threshold law is described in the form $\sigma \propto E^{\eta}$, where $E$ is the energy excess from the threshold and the exponent $\eta \simeq 1.127$, which is similar to the Lyapunov exponent of the classical trajectory of the two electrons astride the potential ridge, namely, $\alpha = \pi/4$ and $\theta_{12} = \pi$. In Wannier's theory the radial motion of the two electrons is decoupled from the angular motion in the quadratic expansion of the potential around the ridge: The potential energy is represented by an inverted parabola in $\alpha$ and by a parabola in $\theta_{12}$. The threshold exponent $\eta$ is determined solely by the radial motion of the two electrons in the vicinity of the potential ridge. Thus, in this section we examine the ionization threshold law using a model in which the angular degrees of freedom are frozen, while the radial degrees of freedom are treated completely. An *a posteriori* justification of using this model in low-energy ionization will be presented by analyzing *ab initio* results for energy as well as angular distributions of the double-continuum states of $^1S^e$ in Sec. III D. We refer to this model as the two-dimensional model [32] because the Schrödinger equation is of two degrees of freedom $\{R, \alpha\}$. In the two-dimensional model, the angular distance between the radial vectors of the individual electrons $\theta_{12}$ is treated as a parameter. Roughly speaking, $\theta_{12}$ determines the curvature of the potential ridge because the expansion of the potential around $\alpha = \pi/4$ up to the quadratic term leads to

$$C \simeq -Z_0(\theta_{12}) - Z_2(\theta_{12})\beta^2, \tag{41}$$

where $\beta = \pi/4 - \alpha$, $Z_0(\theta_{12}) = 2\sqrt{2} - (1-\cos\theta_{12})^{-1/2}$, and $Z_2(\theta_{12}) = 3\sqrt{2} + \cos\theta_{12}(1-\cos\theta_{12})^{-3/2}$. The degree of instability of the radial motion in the vicinity of the potential ridge depends on the curvature. Thus the $\theta_{12}$ dependence of the curvature should be reflected in the threshold law. Indeed, a straightforward implementation of Wannier's theory in the two-dimensional model leads to the $\theta_{12}$-dependent exponent

$$\eta(\theta_{12}) = \sqrt{\frac{1}{16} + \frac{Z_2(\theta_{12})}{Z_0(\theta_{12})}} - \frac{1}{4}, \tag{42}$$

where $\eta(\pi) \simeq 1.127$ coincides with the Wannier exponent. We examine the $\theta_{12}$ dependence of the threshold law in the two-dimensional model by *ab initio* quantal calculations.

Figure 1 shows the numerically obtained total ionization cross sections of the two-dimensional model at low energies. The curvature dependence is evident in the figure. As $\theta_{12}$ decreases, namely, as the curvature of the potential ridge increases, the ionization cross section becomes strongly suppressed near the threshold. This is because the instability of the radial motion near the potential ridge becomes engrossed as the curvature increases; then it becomes more probable that the two electrons prematurely fall into either of the potential valleys at $\alpha \sim 0$ or at $\alpha \sim \pi/2$, leading to excitation [33].

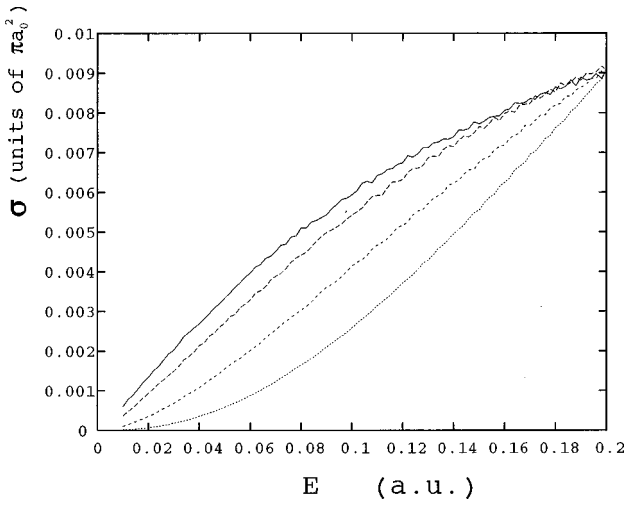


FIG. 1. Variation of the total ionization cross sections of the two-dimensional model with respect to the curvature of the potential *ridge*. The solid line represents the curve for $\theta_{12} = \pi$, the long-dashed line for $\theta_{12} = \pi/2$, the short-dashed line for $\theta_{12} = \pi/3$, and the dotted line for $\theta_{12} = \pi/4$. The cross sections for $\theta_{12} = \pi/2$, $\pi/3$, and $\pi/4$ are normalized to that of $\theta_{12} = \pi$ at $E = 0.2$ a.u.

As the energy increases from the threshold, the ionization cross section rises according to

$$\sigma = E^{\eta(\theta_{12})} G(E), \tag{43}$$

where $\eta(\theta_{12})$ is the $\theta_{12}$-dependent threshold exponent and $G(E)$ is the correction to the energy dependence, which is presumably an analytic function in excess energy around $E^* > 0$,

$$G(E) = \sum_{i=0} a_i (E - E^*)^i. \tag{44}$$

That is, we do not resolve nonanalyticity beyond $E^{\eta}$. We determine the threshold exponent by the least-squares fitting of the numerically obtained cross sections to the analytical form, Eq. (43). In Table I the results are compared with the conjecture based upon Wannier's theory, Eq. (42). The numerical cross sections used in the least-squares fitting lie in the range $0.01 \leqslant E \leqslant 0.2$ a.u. The *ab initio* exponents are in good agreement with the modified Wannier theory. However, the systematic growth of the difference between them for small values of $\theta_{12}$ is seen in the table. One possible interpretation of this is as follows. The curvature of the potential ridge becomes sharper as $\theta_{12}$ becomes smaller, thus the range of validity of the quadratic expansion of the potential becomes narrower. This would imply that for small $\theta_{12}$ the Wannier picture is valid only at vanishingly small energy

TABLE I. Comparison of the numerically obtained threshold exponent with the Wannier-type conjecture, Eq. (42). The numbers in the parentheses are calculated from Eq. (45). The $\lambda_1$ and $\lambda_2$ are obtained by fitting to Eq. (43) and to $\ln\sigma(E)$, respectively.

| $\theta_{12}$ | Wannier | $\lambda_1$ | $\lambda_2$ |
|---|---|---|---|
| $\pi$ | 1.127 (1.354) | 1.124±0.013 | 1.119±0.006 |
| $\frac{\pi}{1.5}$ | 1.177 (1.405) | 1.168±0.014 | 1.156±0.004 |
| $\frac{\pi}{2}$ | 1.294 (1.523) | 1.283±0.016 | 1.304±0.005 |
| $\frac{\pi}{2.5}$ | 1.483 (1.715) | 1.480±0.016 | 1.492±0.005 |
| $\frac{\pi}{3}$ | 1.766 (2.000) | 1.711±0.017 | 1.740 ±0.005 |
| $\frac{\pi}{3.5}$ | 2.169 (2.406) | 2.021±0.021 | 2.073±0.005 |
| $\frac{\pi}{4}$ | 2.740 (2.979) | 2.492±0.023 | 2.514±0.004 |

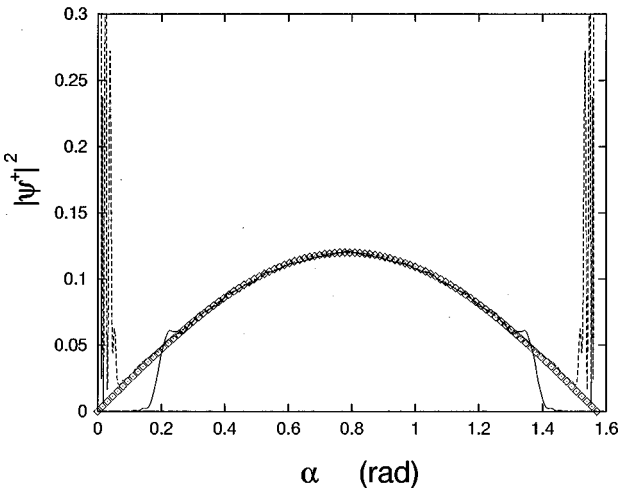


FIG. 2. Squared amplitude of the asymptotic wave function for $E=0.1$ a.u. and $R_M=4000$ a.u. in the case of $\theta_{12}=\pi$. The solid line represents the ionization component and the dashed line the total wave function. Diamonds represent $\sin 2\alpha$ that coincide with the squared amplitude of the ionization component.

excess. Thus, according to the above observations, the systematic discrepancy may reflect that the energies where the fitting is effected are not sufficiently low for small values of $\theta_{12}$.

The two-dimensional model has two degrees of freedom of motion that are coupled, namely, $R$ and $\alpha$. The coupling between the $R$ mode and the $\alpha$ mode stabilizes the radial motions of the two electrons astride the potential ridge. This stabilization phenomenon may be interpreted as an inertial effect, akin to the Coriolis force [34]. In Table I the numbers in parentheses indicate the threshold exponents that are obtained by neglecting the coupling,

$$\tilde{\eta}(\theta_{12})=\sqrt{\frac{Z_2(\theta_{12})}{Z_0(\theta_{12})}}. \tag{45}$$

The stabilization effect is evidently seen in the threshold exponent. The exponent without the coupling is always larger than that with the coupling. This indicates that the ionization cross sections that are obtained by neglecting the coupling become suppressed near the threshold much more so than those that are obtained by including the coupling.

### B. Energy distribution of double continuum states for the two-dimensional model

Wannier's theory presumes that in the threshold ionization two electrons escape from the small region with equal energies, thus the energy distribution of the two electrons would localize at $\epsilon_1=\epsilon_2$ at the initial stage of escaping. However, the escaping electrons continue to exchange their kinetic energy under the influence of the long-range Coulomb force between them, thus the energy distribution evolves until they attain the asymptotic region where the kinetic energy dominates over the Coulomb interaction energy. Thus the distribution finally established in the asymptotic region would differ from that at the initial stage of escaping. Classical [13,17,18], semiclassical [19], and quantal calculations resorting to some semiclassical ansatz [20,21] provided an almost uniform energy distribution at low energies. Here we examine the energy distribution within the two-dimensional model of $\theta_{12}=\pi$ by carrying out fully quantal calculations.

Figure 2 illustrates the squared amplitude of the asymptotic wave function as well as its ionization component at $E=0.1$ a.u. for $R_M=4000$ a.u. In this figure the wave functions are folded into the representation in terms of the hyperspherical channel functions, that is, $\Sigma_n\Phi_n\langle\Phi_n|\psi^+\rangle$. Near the potential valley, namely, $\alpha\sim 0,\pi/2$, the squared amplitude of the total wave function has a rapid oscillation that corresponds to the formation of Rydberg states of the target hydrogen, whereas apart from the potential valley the squared amplitude shows a quite smooth distribution that corresponds to the ionization component. The rapid decline of the ionization component near the potential valley indicates that the valley is strongly absorptive for the ionization component. Thus we may conclude that there is no revival from the potential valley back to the ridge in the asymptotic region. In classical terms, the trajectories that prematurely fall into the valley always lead to excitation. In Wannier's original paper, a similar statement was made as a basis of his reasoning in terms of ridge trajectories of two electrons. Moreover, it may indicate some classical feature of the asymptotic wave function, namely, that the ionization component is well localized with respect to $\alpha$ forming a wave packet.

In the figure it is also evident that the squared amplitude of the ionization component is well described by $\sin 2\alpha$ except for the potential valley. The point is that the correct behavior of an ionization wave function is not uniform with respect to $\alpha$: The uniformity that is derived from the local solutions of Peterkop and Rau just represents the local behavior in the vicinity of $\alpha=\pi/4$. Using Eq. (40) and taking the phase-space factor $\sin 2\alpha$ into account, we find that the good fit of the squared amplitude of the ionization component to $\sin 2\alpha$ indicates that the energy distribution is uni-

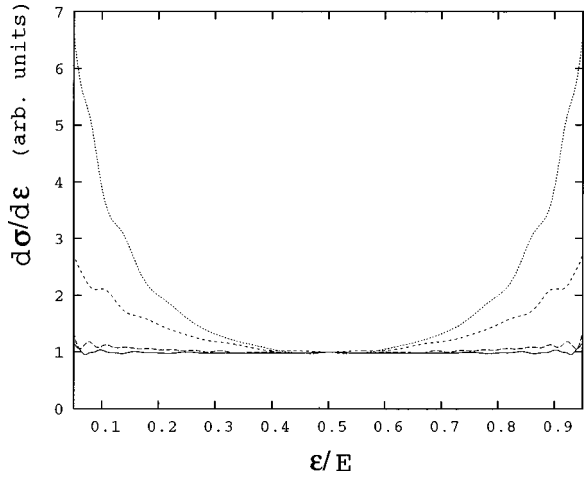


FIG. 3. Energy distribution of the two electrons in the case of $\theta_{12}=\pi$. The solid line is for $E=0.1$ a.u., the long-dashed line for $E=0.5$ a.u., the short-dashed line for $E=2.0$ a.u., and the dotted line for $E=5.0$ a.u. The distributions are normalized to unity, where both of the electrons share the available energy evenly. The distribution appears uniform at $E=0.1$ a.u. on this scale.

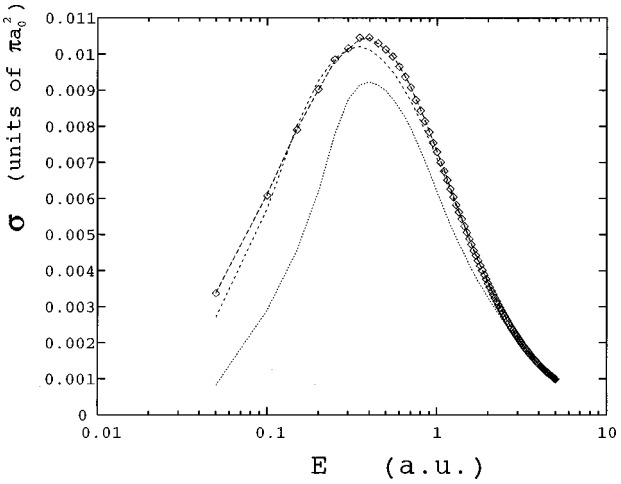


FIG. 4. Convergence of the total ionization cross sections with respect to the number of hyperspherical channels $N$ in the case of $\theta_{12}=\pi$. Diamonds represent the results for $N=20$, the long-dashed line for $N=13$, the short-dashed line for $N=12$, and the dotted line for $N=11$.

form. Figure 3 shows the energy distribution obtained from the squared amplitude of the ionization wave function using Eq. (40). In the figure it is evident that the energy distribution becomes uniform as the energy decreases. Thus we may infer that after leaving the small region the energy distribution of the two electrons continuously diffuses from where $\epsilon_1=\epsilon_2$ and becomes uniform asymptotically.

It would be intriguing to consider the Temkin-Poet (TP) model for further investigation of the energy distribution at low energies. In the TP model the interelectronic interaction potential is replaced by the monopole term, thus the potential has a cusp at the ridge. It is expected that the cusp ridge has a quite different effect on threshold ionization when compared to the inverted-parabola ridge as in the two-dimensional model. While the inverted-parabola ridge represents a fixed point in the classical phase space, the cusp ridge does not. Thus the energy distribution of the TP model [35] at low energies would be considerably different from that of the two-dimensional model. Our pilot calculations for the TP model indeed indicate marked differences and will be reported elsewhere.

### C. Role of the potential ridge in low-energy ionization

We examine the convergence of the present calculations with respect to the number of hyperspherical channels included in the calculations as well as to the hyperradial distances where the matching procedure is effected. We limit the analysis to $\theta_{12}=\pi$. The essential role of the potential ridge manifests itself in the convergence.

First, we examine the convergence with respect to the number of hyperspherical channels included in the calculations, while the matching hyperradius is always fixed. Thus the analysis would reveal the ionization dynamics within the interior region bounded by the matching hyperradius. Figure 4 illustrates the convergence of the total ionization cross sections at representative energies as a function of the number of hyperspherical channels for the matching hyperradius $R_M=500$ a.u. The cross sections vary rather sharply as the number of channels increases and then suddenly convergence obtains at all energies. In the figure, this sudden convergence is particularly marked at low energies, while at high energies the cross sections are almost unaltered. It suggests that there is a specific ionization mechanism that dominates in low-energy ionization. Let us argue in favor of the successive promotion via the potential ridge [36]. Figure 5 shows the adiabatic potential curves that are associated with the adiabatic channels up to where the matching is effected. It is evident in the figure that the number of adiabatic channels required for convergence coincides with the number of adiabatic potential curves that possess avoided crossings along the potential ridge. It may be taken as direct evidence of the successive promotion to ionization via the ridge.

Next we examine the convergence with respect to the matching hyperradial distances. It is expected that the two

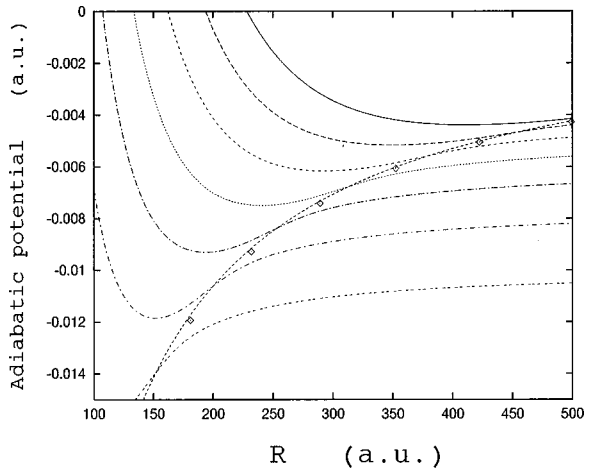


FIG. 5. Adiabatic potential curves in the case of $\theta_{12}=\pi$. The solid line represents the adiabatic potential curve that is associated with the 13th channel. The potential ridge is represented by the dashed curve, which monotonically rises from the bottom of the figure across the potential curves. Diamonds represent the middle points of energy gaps between the potential curves at where the avoided crossings occur.

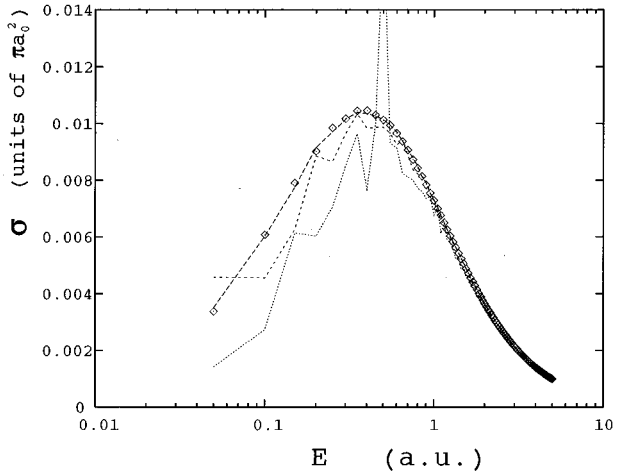


FIG. 6. Convergence of the total ionization cross section with respect to the matching hyperradius $R_M$ in the case of $\theta_{12}=\pi$. Diamonds represent the result for $R_M=500$ a.u., the long-dashed line for $R_M=300$ a.u., the short-dashed line for $R_M=100$ a.u., and the dotted line for $R_M=50$ a.u. Convergence seems to be achieved at $R_M \geqslant 300$ a.u. at all energies of $E \geqslant 0.05$ a.u.

electrons hardly exchange their kinetic energies at large hyperradial distances where the total kinetic energy dominates over the Coulomb interaction energy. Thus, at finite energies above the threshold the ionization process becomes completed by reaching some large but finite hyperradius. Figure 6 illustrates the convergence of the ionization cross section with respect to the matching hyperradius. In the figure the cross sections for each matching hyperradius have already converged with respect to the number of hyperspherical channels. It is evident that the cross section at a finite energy converges with a finite hyperradius. However, the convergence becomes slower as the energy decreases. This is because at low energies the energy exchange between the two electrons takes place over up to even larger hyperradial distances; the distances may be scaled proportionally to $E^{-1}$, as often argued in the manner of Wannier.

### D. Angular correlations of two electrons in double-continuum states: $^1S^e$ symmetry

In addition to $R$ and $\alpha$, realistic three-body systems have one more internal degree of freedom that represents the motion with respect to the interelectronic angular distance, namely, $\theta_{12}$. In this section we neglect the orientational degree of freedom that can be described by the Euler angles. We consider $^1S^e$ symmetry only.

In the present calculations the angular part of electronic states are represented in terms of individual angular-momentum states $(l_1,l_2)$, where $l_1=l_2=l$ since $J=0$. Thus we first examine the convergence of ionization cross sections with respect to the individual angular momentum $l$. Figure 7 illustrates the convergence of partial ionization cross sections with respect to $l_{max}$, where $l_{max}$ is the maximum angular-momentum state included in the calculations. In the figure the partial ionization cross sections for $l \leqslant 2$ almost converge when $l_{max}=5$. To obtain converged results for higher $l$ components, we need to increase $l_{max}$; however, as the angular momentum $l$ increases the contribution to the ionization cross section decreases rapidly unless the total energy is

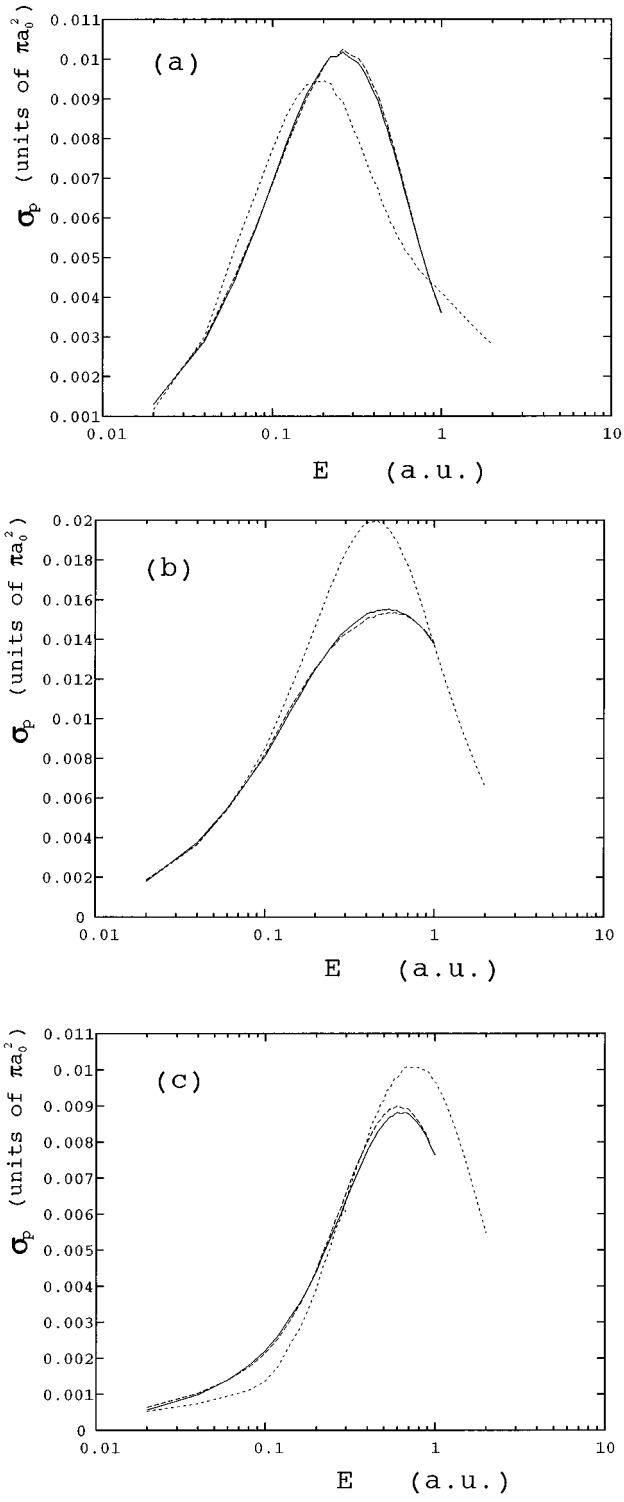


FIG. 7. Partial ionization cross sections with respect to individual angular-momentum states in the case of $^1S^e$ for (a) $l=0$, (b) $l=1$, and (c) $l=2$. The solid line represents the result for $l_{max}=5$, the long-dashed line for $l_{max}=4$, and the short-dashed line for $l_{max}=2$.

close to the threshold energy. In Fig. 8 the contribution from each angular-momentum state is identified. The $p$-wave component $(l=1)$ dominates over other angular-momentum states and this contribution increases as the energy increases, while the contributions from the other angular-momentum

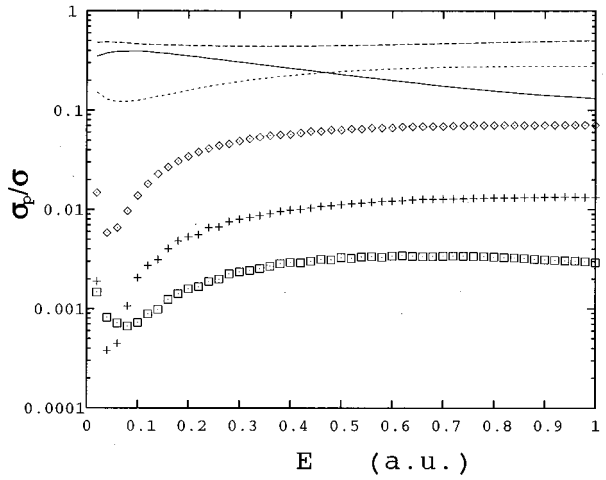


FIG. 8. Contribution of individual angular-momentum states to the total ionization cross section of $^1S^e$. The solid line represents $l=0$, the long-dashed line $l=1$, the short-dashed line $l=2$, diamonds $l=3$, crosses $l=4$, and squares $l=5$.

states become saturated or suppressed. This suggests that at high energies the dipolelike transition dominates the ionization. Below $E=0.1$ a.u. a qualitative change in the behavior of each component is seen in the figure; the contributions of large-angular-momentum states begin to grow. This may suggest strong interelectronic correlations with respect to the angular distance of the two electrons $\theta_{12}$ near the threshold.

Wannier's theory presumes that near the threshold the two electrons escape from the small region in opposite directions leaving the nucleus in the middle of them, namely, $\theta_{12}\sim\pi$. The conjecture is intuitively reasonable because it is expected that the long-range interelectronic Coulomb repulsion force pushes the escaping electrons away from each other. Using an advanced photon source, angular distributions of the two electrons in double-continuum states were measured in double photoionization of helium near the threshold [37] and recently recoil ion momentum spectroscopy was carried out in double photoionization of helium [38]. These experiments showed that near the threshold the angular distribution of the two electrons indeed localizes around $\theta_{12}=\pi$.

Now let us demonstrate *ab initio* results for angular as well as energy distributions of the two electrons in double-continuum states. Figure 9 illustrates the angular and the energy distributions of the two electrons in the electron-impact ionization of hydrogen ($^1S^e$). These distributions are obtained from ionization wave functions using Eq. (40). The ionization wave functions are folded into the representation in terms of the hyperspherical channel functions as was done in the two-dimensional model. At the lowest energy, $E=0.2$ a.u., it is evident that the angular distribution is localized near $\theta_{12}=\pi$ and the energy distribution is almost uniform. The distribution is seen to be almost constant with respect to $\epsilon$ at all values of $\theta_{12}$ and shows a quite simple behavior. Within the validity of the stationary-phase approximation, this indicates that at low energies the $\alpha$ motion of the two electrons in double-continuum states is well decoupled from the $\theta_{12}$ motion. It may be regarded as an *a posteriori* justification of using the two-dimensional model in low-energy ionization. As the energy increases, the amplitude at the potential ridge becomes suppressed; the angular distribution at small interelectronic angular distances grows and the energy distribution becomes nonuniform. At the highest energy, $E=5.0$ a.u., the distribution shows a quite different feature

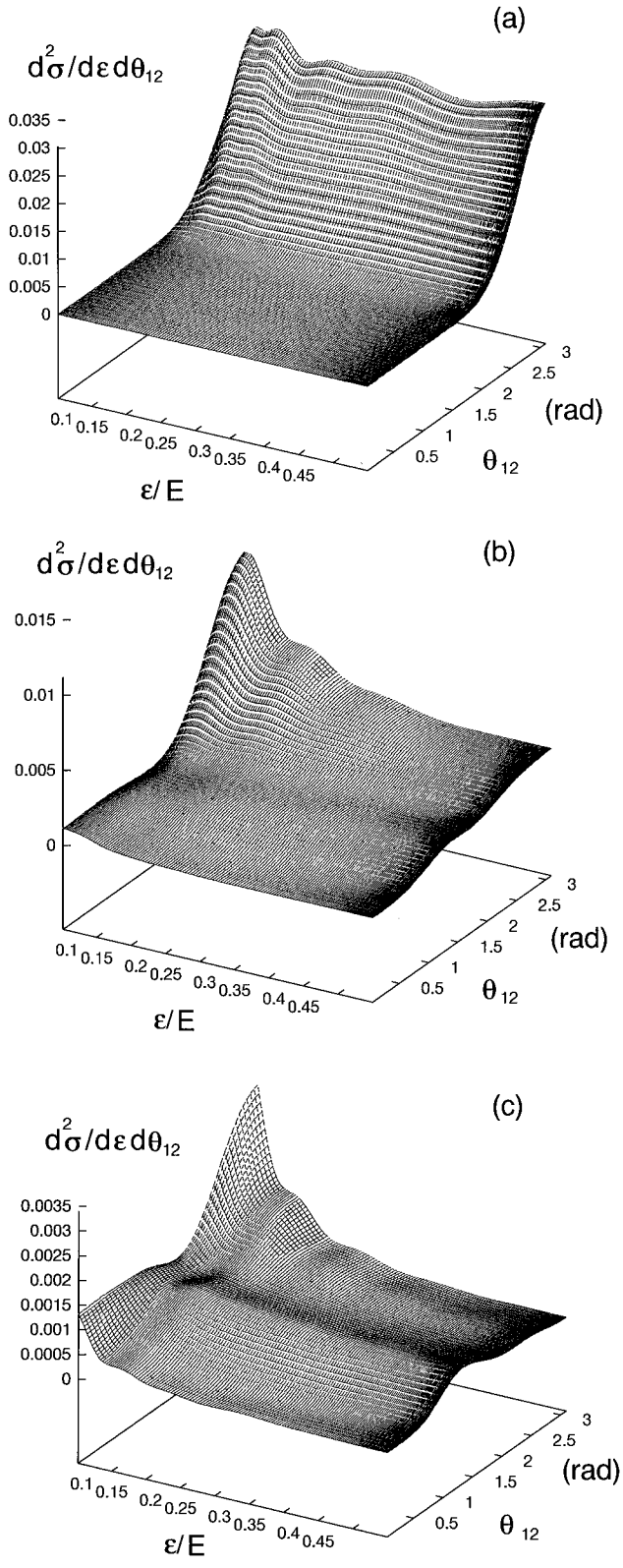


FIG. 9. Energy as well as angular distribution of the two electrons in electron-impact ioinization of hydrogen in the case of $^1S^e$ for (a) $E=0.2$ a.u., (b) $E=2.0$ a.u., and (c) $E=5.0$ a.u. Note the manifestation of the binary-encounter peak at $\theta_{12}\sim\pi/2$ in (c).

TABLE II. List of individual angular-momentum pairs for each symmetry specified by $\{J,S,\Pi\}$. The number $N$ in the parentheses represents the number of coupled hyperspherical channels.

| | | | | | | |
|---|---|---|---|---|---|---|
| $^{1,3}S^e$ ($N=100$) | (0,0) | (1,1) | | (2,2) | | |
| $^{1,3}P^o$ ($N=100$) | (0,1) | (1,2) | | (2,3) | | |
| $^{1,3}D^e$ ($N=80$) | (0,2) | (1,1) | (1,3) | (2,2) | (2,4) | |
| $^{1,3}F^o$ ($N=80$) | (0,3) | (1,2) | (1,4) | (2,3) | (2,5) | |
| $^{1,3}G^e$ ($N=80$) | (0,4) | (1,3) | (1,5) | (2,2) | (2,4) | (2,6) |
| $^{1,3}H^o$ ($N=80$) | (0,5) | (1,4) | (1,6) | (2,3) | (2,5) | (2,7) |
| $^{1,3}I^e$ ($N=80$) | (0,6) | (1,5) | (1,7) | (2,4) | (2,6) | (2,8) |
| $^{1,3}7^o$ ($N=80$) | (0,7) | (1,6) | (1,8) | (2,5) | (2,7) | (2,9) |
| $^{1,3}8^e$ ($N=80$) | (0,8) | (1,7) | (1,9) | (2,6) | (2,8) | (2,10) |
| $^{1,3}9^o$ ($N=80$) | (0,9) | (1,8) | (1,10) | (2,7) | (2,9) | |
| $^{1,3}10^e$ ($N=80$) | (0,10) | (1,9) | | (2,8) | (2,10) | |

from that of the lowest energy. The classical binary-encounter peak manifests itself near $\theta_{12}=\pi/2$ in the angular distribution. In the case that one of the electrons possesses the bulk of the available energy, the angular distribution around $\theta_{12}=0$ and $\pi$ becomes enhanced, suggesting that the dipolelike mechanism manifests itself in the ionization. Strictly, speaking, the angular distribution peaks at $\theta_{12}=\pi$ due to the Coulomb repulsion force exerted from the fast electron. As regards the relative importance of the dipolelike mechanism and the binary-encounter one, the figure indicates that the amplitude of the former mechanism totally dominates over that of the latter at high energies.

### E. Comparison with experimental measurements as well as other theories: Spin-averaged total ionization cross section and spin asymmetry

In this section we demonstrate the validity of the present theoretical method with regard to spin-averaged total ionization cross sections as well as the spin asymmetry in the low- to intermediate-energy range comparing with experimental measurements as well as other theoretical results. In the present calculations we employ the partial-wave expansion with respect to the total angular momentum $J$. In Table II individual angular-momentum pairs $(l_1,l_2)$ and the number of hyperspherical channels included in each partial wave are listed. Here we examine convergence of the partial-wave expansion with respect to $J$. Figure 10 illustrates the contribution of each partial-wave component to the ionization cross section. At the lowest energy, $E=0.1$ a.u., small-$J$ components dominate the ionization cross section. On the contrary, at the highest energy, $E=2.0$ a.u., the distribution extends over large $J$, indicating that the partial-wave expansion with respect to $J$ becomes disadvantageous at high energies. In calculating the total ionization cross sections, contributions from $J>10$ are extrapolated: The net contribution from $J>10$ is less than 10% at $E=2.0$ a.u.

Figure 11 illustrates comparison of the spin-averaged total ionization cross section with experiments as well as the convergent-close-coupling (CCC) result of Bray and Stelbovics [2] in the energy range $E\leqslant 2.0$ a.u. The excellent agreement with the experiment by Shah *et al.* [39] is seen in the figure. Near the threshold, however, the present result indicates a noticeable departure from the experiment by McGowan and Clarke [10]. The incomplete agreement may be partly due to the finite energy resolution in the experiment and partly due to the normalization of the experimental cross sections. Indeed, for the energy dependence of the cross sec-

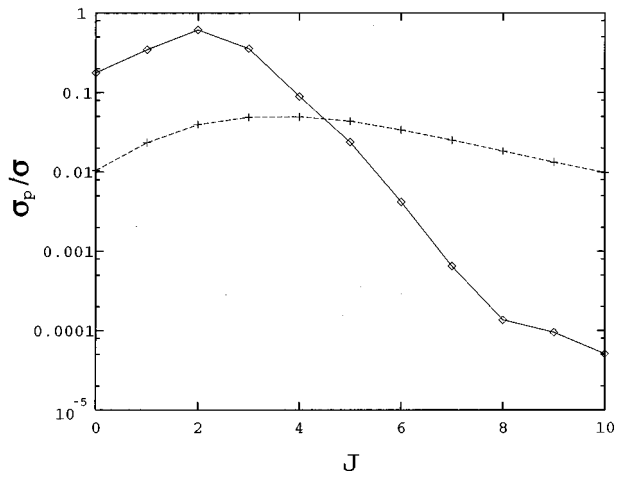


FIG. 10. Contribution of each partial wave component to the ionization cross section. The solid line is for $E=0.1$ a.u. and the dashed line for $E=2.0$ a.u.

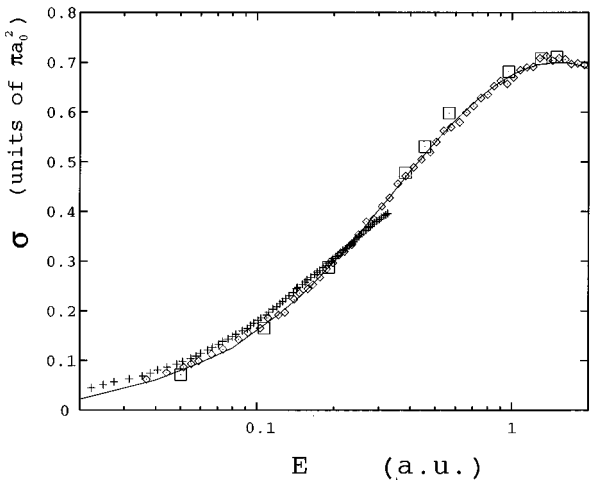


FIG. 11. Spin-averaged total ionization cross sections. The solid line represents the present result, diamonds the experiment by Shah *et al.* [39], crosses the experiment by McGowan and Clarke [10], and open squares the convergent-close-coupling method of Bray and Stelbovics [2].

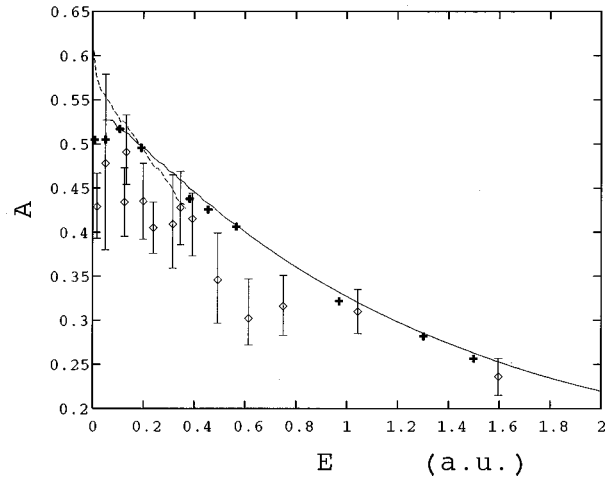


FIG. 12. Comparison of spin asymmetry with experiment as well as other theories. The solid line represents the present result, the dashed line the hidden-crossing theory of Macek *et al.* [14], crosses the convergent-close-coupling method, and diamonds with error bars the experiment by Fletcher *et al.* [40].

tion the present result agrees well with both experimental results. The CCC result almost coincides with the present result at all energies in the figure. Since both theoretical methods are completely different, the complete agreement is convincing.

Figure 12 illustrates a comparison of the spin asymmetry of the ionization cross section with experiment as well as other theories. The spin asymmetry represents the difference in contribution between the singlet spin state and the triplet spin state in the form

$$A=\frac{\sigma_S-\sigma_T}{\overline{\sigma}}, \tag{46}$$

where $\sigma_S$ and $\sigma_T$ represent the ionization cross section of the singlet spin state and that of the triplet spin state, respectively, and $\overline{\sigma}$ represents the spin-averaged total ioinization cross section. The present result agrees very well with the CCC result [2], except near the threshold: The CCC result indicates a rapid decline near the threshold. The hidden-crossing result by Macek *et al.* [14] noticeably disagrees with both of the CCC result and ours at moderately low energies. Near the threshold, the hidden-crossing result rapidly increases, whereas the present result does not. Besides near the threshold, the disagreement with the hidden-crossing result at moderately low energies is hardly understandable because the present calculations converge in this energy range well. Because they are based upon completely different theoretical schemes, the complete agreement with the CCC result in this energy range is convincing. The present result totally agrees with the experimental result of Fletcher *et al.* [40], while all theories predict values within the experimental error bars. Strictly speaking, the theoretical results are always in the upper side of the experimental error bars. We postpone critical examination of other theories. Let us note, however, that the statistical uncertainty in the experiment is very large at low energies. The spin asymmetry of the $S$ state alone is doomed to converge to 1 at the threshold; therefore, we may at least conclude that at the threshold total-angular-momentum states $J>0$ have rather large contributions to ionization because the spin asymmetry seems to converge to a value apparently smaller than 1 at the threshold.

## IV. CONCLUSION

In summary, we presented a theoretical method for the *ab initio* treatment of interelectronic correlations in double-continuum states. In the method, the strong interelectronic correlations are represented by the hyperspherical channel functions and accurate numerical solutions of the two-electron atomic Schrödinger equation are obtained by means of the smooth-variable-discretization method in combination with the $R$-matrix propagation method. The double-continuum boundary condition is represented by matching the numerical solutions to asymptotic solutions that are described by superpositions of approximate asymptotic channel functions.

Armed with the efficient and stable scheme, we have presented *ab initio* results on the ionization of the electron-hydrogen collision. Our theoretical results for the two-dimensional model definitively support Wannier's threshold law. Energy distributions of double-continuum states become uniform at low energies, indicating that interelectronic radial correlations become suppressed asymptotically due possibly to some diffusive mechanisms around the potential ridge. Analyzing the convergence of the present calculations led to confirming that the potential ridge plays an essential role in propagating the ionization flux at low energies. At low energies, angular distributions in double-continuum states of $^1S^e$ localize where the interelectronic angular distance $\theta_{12}=\pi$. As the energy increases, the classical binary-encounter as well as the dipole-transition mechanisms become apparent in angular distributions. Our theoretical results of spin-averaged total ionization cross sections as well as the spin asymmetry show good agreement with experimental measurements as well as the convergent-close-coupling result at low to intermediate energies. However, regarding the spin asymmetry, there is a noticeable disagreement with the hidden-crossing result at moderately low energies.

The present theoretical method is capable of handling the ionization process in a wide energy range and also provides a unique perspective to the study of interelectronic correlations in double-continuum states. Thus the method may be applied in the future to various atomic processes that involve double-continuum states.

## ACKNOWLEDGMENTS

We thank Dr. Matsuzawa for his continuing encouragement and interest in the problem. We also thank Dr. O. I. Tolstikhin for instructive discussions on the SVD method, Dr. P. F. O'Mahony for providing us with his own version of the $R$-matrix propagation code, and Dr. J. H. Macek and Dr. I. Bray for kindly providing their own numerical data of ionization cross sections. We are grateful to Dr. K. Hino, Dr.

J. Z. Tang, and Dr. T. Morisita for useful discussions. D. K. thanks all colleagues in the Matsuzawa-Watanabe Laboratory and acknowledges gratefully the financial support provided by the Japan Society for Promotion of Science. S. W. acknowledges with gratitude partial financial support from the Matsuo Foundation. The computations were partially carried out on the supercomputer VPP500 in RIKEN. This work was supported in part by a Grant-in-Aid for Exploratory Research, Ministry of Education, Science and Culture, Japan.

[1] G. Peach, Proc. Phys. Soc. **87**, 381 (1969).
[2] I. Bray and A. T. Stelbovics, Phys. Rev. Lett. **70**, 746 (1993); and private communication.
[3] G. Wannier, Phys. Rev. **90**, 817 (1953).
[4] R. Peterkop, J. Phys. B **4**, 513 (1971); R. Peterkop, *Theory of Ionization of Atom by Electron Impact* (Colorado Associated University Press, Boulder, 1977).
[5] A. R. P. Rau, Phys. Rev. A **4**, 207 (1971).
[6] H. Klar and W. Schlecht, J. Phys. B **9**, 1699 (1976); C. H. Greene and A. R. P. Rau, *ibid.* **16**, 99 (1983).
[7] J. M. Feagin, J. Phys. B **17**, 2433 (1984).
[8] D. S. Crothers, J. Phys. B **19**, 463 (1986).
[9] S. Watanabe, J. Phys. B **24**, L39 (1991); A. K. Kazansky and V. N. Ostrovsky, *ibid.* **25**, 2121 (1992).
[10] J. W. McGowan and E. M. Clarke, Phys. Rev. **167**, 43 (1968).
[11] S. Cvejanović and F. H. Read, J. Phys. B **7**, 1841 (1974).
[12] D. Proulx and R. Shakeshaft, Phys. Rev. A **48**, R875 (1993).
[13] J. M. Rost, Phys. Rev. Lett. **72**, 1998 (1994).
[14] J. H. Macek, S. Yu. Ovchinnikov, and S. V. Pasovets, Phys. Rev. Lett. **74**, 4631 (1995); J. H. Macek and S. Yu. Ovchinnikov, Phys. Rev. A **54**, 544 (1996).
[15] P. Hammond, F. H. Read, S. Cvejanović, and G. C. King, J. Phys. B **18**, L141 (1985).
[16] J. M. Feagin, J. Phys. B **28**, 1495 (1995).
[17] I. Vinkalns and M. Gailitis, *Abstracts of the Fifth International Conference on the Physics of Electronic and Atomic Collisions, Leningrad, 1967*, edited by I. P. Flaks and E. S. Solov'ev (Nauka, Leningrad, 1967), p. 648.
[18] F. H. Read, J. Phys. B **17**, 3965 (1984).
[19] A. K. Kazansky, V. N. Ostrovsky, and L. Yu. Sergeeva, J. Phys. B **27**, 5197 (1994).
[20] R. Peterkop and A. Liepinsh, J. Phys. B **14**, 4125 (1981).
[21] D. Pont and R. Shakeshaft, J. Phys. B **28**, L571 (1995).
[22] O. I. Tolstikhin, S. Watanabe, and M. Matsuzawa, J. Phys. B **29**, L389 (1996).
[23] K. L. Baluja, P. G. Burke, and L. A. Morgan, Comput. Phys. Commun. **27**, 299 (1982).
[24] D. Kato and S. Watanabe, Phys. Rev. Lett. **74**, 2443 (1995).
[25] J. H. Macek, J. Phys. B **1**, 831 (1968).
[26] J. C. Light, I. P. Hamilton, and J. V. Lill, J. Chem. Phys. **82**, 1400 (1985).
[27] S. Watanabe and H. Komine, Phys. Rev. Lett. **67**, 3227 (1991); J. Z. Tang, S. Watanabe, and M. Matsuzawa, Phys. Rev. A **46**, 2437 (1992); A. Igarashi and N. Toshima, *ibid.* **50**, 232 (1994); Y. Zhou and C. D. Lin, J. Phys. B **27**, 5065 (1994).
[28] K. Hino, A. Igarashi, and J. H. Macek, Phys. Rev. A **56**, 1038 (1997).
[29] J. C. Light and R. B. Walker, J. Chem. Phys. **65**, 4272 (1976).
[30] Recently, hidden-crossing theory was applied for the representation of electron-impact ionization of the hydrogen atom using complex-valued adiabatic channels [14].
[31] W. H. Press, S. A. Teukolsky, W. T. Vettering, and B. P. Flannery, *Numerical Recipes in FORTRAN* (Cambridge University Press, Cambridge, 1992), pp. 51–63.
[32] D. Kato and S. Watanabe, J. Phys. B **29**, L779 (1996); S. Watanabe, D. Kato, and M. Matsuzawa, Comments At. Mol. Phys. **33**, 95 (1996).
[33] It is argued in Wannier's theory that the classical trajectories that prematurely fall into the potential *valleys* always lead to excitation and there is no revival to the ionization from the excitation paths.
[34] A. R. P. Rau (unpublished).
[35] J. H. Macek and W. Ihra, Phys. Rev. A **55**, 2024 (1997).
[36] U. Fano, J. Phys. B **7**, L401 (1974); Phys. Rev. A **22**, 2660 (1980).
[37] O. Schwarzkopf, B. Krässig, J. Elmigen, and V. Schmidt, Phys. Rev. Lett. **70**, 3008 (1993); A. Huetz, P. Lablanquie, L. Andric, P. Selles, and J. Mazeau, J. Phys. B **27**, L13 (1994).
[38] R. Döner, J. M. Feagin, C. L. Cocke, H. Bräuning, O. Jagutzki, M. Jung, E. P. Kanter, H. Khemliche, S. Kravis, V. Mergel, M. H. Priot, H. Schmidt-Böcking, L. Spielberger, J. Ullrich, M. Unversagt, and T. Vogt, Phys. Rev. Lett. **77**, 1024 (1996).
[39] M. B. Shah, D. S. Elliot, and H. B. Gilbody, J. Phys. B **20**, 3501 (1987).
[40] G. D. Fletcher, M. J. Alguard, T. J. Gay, V. W. Hughes, P. F. Wainwright, M. S. Lubell, and W. Raith, Phys. Rev. A **31**, 2854 (1985).